A gap in the Indo-Pacific warm pool over the South China Sea in boreal winter: Seasonal development and interannual variability

Qinyu Liu and Xia Jiang

Physical Oceanography Laboratory and Ocean-Atmosphere Interaction and Climate Laboratory, Ocean University of China, Qingdao, China

Shang-Ping Xie

International Pacific Research Center and Department of Meteorology, University of Hawaii, Honolulu, Hawaii, USA

W. Timothy Liu

Jet Propulsion Laboratory, Pasadena, California, USA

Received 24 October 2003; revised 15 January 2004; accepted 3 May 2004; published 13 July 2004.

[1] The Indo-Pacific warm water pool in boreal winter shows a conspicuous gap over the South China Sea (SCS) where sea surface temperature (SST) is considerably lower than over the oceans both to the west and east. The formation mechanisms for the climatology and interannual variability of SCS SST in boreal winter are investigated using a suite of new satellite measurements. The winter SCS is divided into two parts by the axis of the maximum northeasterly monsoonal winds. The positive wind curl in the southeastern half of the ocean drives a cyclonic gyre circulation in the deep basin. As its western boundary current, an intense southward flow is found south of Vietnam on the continental slope separating the Sunda Shelf to the west and the deep SCS basin to the east. This slope current exceeds 0.5 m s^{-1} in speed and advects cold water from the north. This cold advection results in a distinct cold tongue in the winter SST climatology. Both the slope current and the cold tongue are strongest in November to February. This winter cold tongue displays considerable interannual variability that is highly correlated with eastern equatorial Pacific SST. In an El Niño the winter monsoon weakens, causing the SCS ocean circulation to spin down. The reduced western boundary current and its thermal advection result in a warming in the SCS winter cold tongue. Both SST variance and its correlation with the El Niño-Southern Oscillation peak along the climatological cold tongue indicate that ocean dynamics are an important player in SCS climate variability. *INDEX TERMS:* 3339 Meteorology and Atmospheric Dynamics: Ocean/atmosphere interactions (0312, 4504); 4512 Oceanography: Physical: Currents; 4522 Oceanography: Physical: El Niño; 4576 Oceanography: Physical: Western boundary currents; 4215 Oceanography: General: Climate and interannual variability (3309); *KEYWORDS:* Indo-Pacific warm pool, South China Sea, cold tongue

Citation: Liu, Q., X. Jiang, S.-P. Xie, and W. T. Liu (2004), A gap in the Indo-Pacific warm pool over the South China Sea in boreal winter: Seasonal development and interannual variability, *J. Geophys. Res.*, *109*, C07012, doi:10.1029/2003JC002179.

1. Introduction

[2] The South China Sea (SCS) has a deep basin and is the largest marginal sea in Southeast Asia. In this semi-enclosed basin, water exchanges with the western Pacific mainly through the Luzon Strait (Figure 1). The upper ocean circulation within SCS displays a strong seasonal cycle in response to the SCS monsoons that are southwesterly and northeasterly in summer and winter, respectively [*Wyrki*, 1961; *Xu et al.*, 1980; *Shaw and Chao*, 1994; *Chu et al.*, 1999; *Liu et al.*, 1997; *Q. Liu et al.*, 2001]. In this paper, seasons always refer to those for the Northern Hemisphere; for example, winter of 2000 refers to the 3 months of December 1999 and January and February 2000. Observations using satellite altimetry [*Shaw et al.*, 1999; *Ho et al.*, 2000; *Li et al.*, 2000], historical temperature and salinity measurements [*Qu*, 2000], and numerical models [*Shaw and Chao*, 1994; *Chu et al.*, 1999; *Yang et al.*, 2002] indicate that the basin-scale circulation of the upper SCS is generally cyclonic in winter in response to the northeasterly monsoon and reverses to anticyclonic in summer accompanying the southwest monsoon. *Liu and Xie* [1999] discuss the responses of SCS sea surface temperature (SST) and sea surface height to monsoon variations in surface heat flux and wind stress. The

0148-0227/04/2003JC002179$09.00

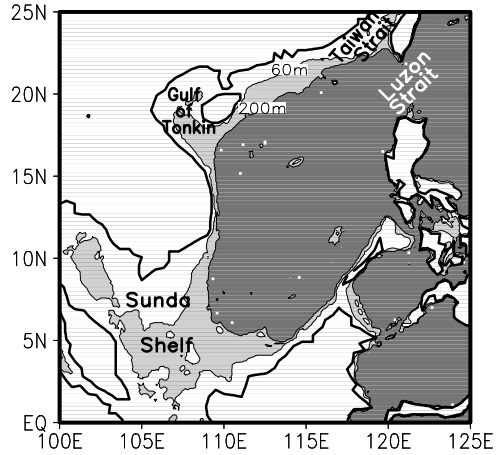

Figure 1. Bathymetry of the South China Sea. Regions deeper than 60 (200) m are denoted by light (dark) shading.

adjustment of the SCS circulation to monsoonal winds can be understood in terms of Rossby wave dynamics [*Z. Liu et al.*, 2001]. The Rossby waves of the gravest baroclinic mode travel across the basin in 1–2 months, leaving the upper ocean in a quasi-steady equilibrium with the annual monsoon forcing.

[3] The SCS is located within the general area of the so-called Indo-Pacific warm water pool that anchors the largest atmospheric convection center. The 28°C SST contour is often used as the boundary for the Indo-western Pacific warm pool. In winter, the SCS is generally colder (~2°C) than the Indian or western Pacific on either side (Figure 2a). While the 28°C SST contour is located around 15°N and 10°N over the western Pacific and Indian Oceans, respectively, SST is below 28°C over most of the SCS. In the middle southern SCS a tongue of cold water penetrates deep into the south in 105°~110°E, creating a conspicuous gap in the Indo-Pacific warm pool. At 7°N, SST is 28.5°C or above in both the Indian and Pacific Oceans, but it is only 26°C in the SCS cold tongue. This SCS cold tongue seems to exert a strong influence on the atmosphere, creating a persistent break in atmospheric convection that occupies the Indo-Pacific region south of 10°N in boreal winter (Figure 2b). Furthermore, annual harmonic of SST reaches a pronounced maximum in this cold tongue, indicating that it is an important element of seasonal variations in SCS climate (Figure 3). To our knowledge, the mechanism for the formation of this winter cold tongue in the SCS has not been discussed in the literature.

[4] The present study examines the seasonal development of this SCS cold tongue and investigates the ocean-atmospheric conditions that lead to its formation and interannual variability. We take advantage of new high-resolution satellite observations that reveal the structure of the vast oceans and the overlying atmosphere in detail that was never possible before [*Xie*, 2004]. In a closely related study, *Xie et al.* [2003] investigate summer SCS climate and demonstrate the usefulness and potential of satellite observations for studying this marginal sea. The present study focuses instead on winter climate. We show that the SCS cold tongue in winter results from the cold advection by the

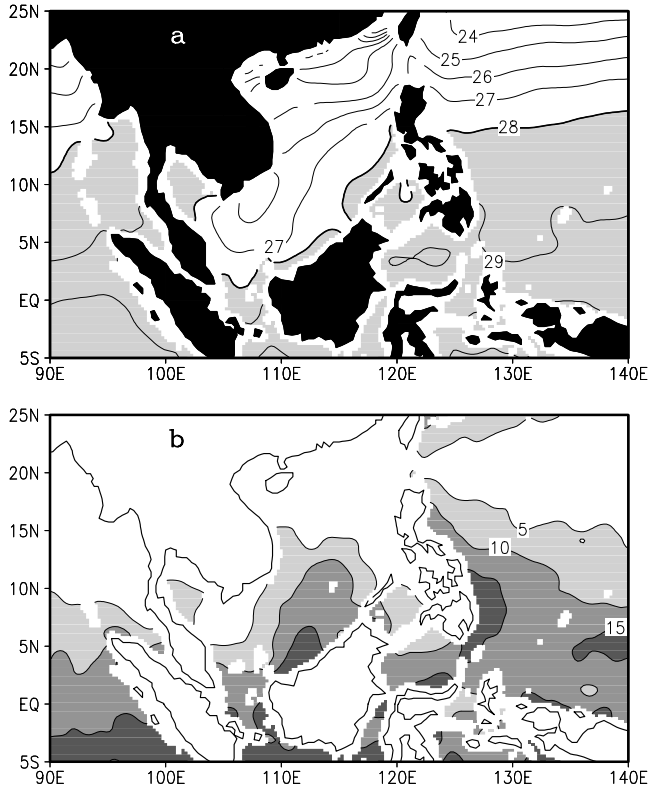

Figure 2. (a) TMI SST (contours at 1°C intervals; shaded for SST ≥28°C) and (b) precipitation rate (mm d^{-1}), averaged for five winters of 1998–2002.

southward western boundary current along the continental slope between the Sunda Shelf and the deep SCS to the east. (The Sunda Shelf is the extensive continental shelf south of Indochina and east of Malay Peninsula, including the Gulf of Thailand.) This cold tongue displays large interannual variability in association with El Niño-Southern Oscillation (ENSO).

[5] The rest of the paper is organized as follows. Section 2 briefly describes the data sets. Sections 3 and 4 examine the

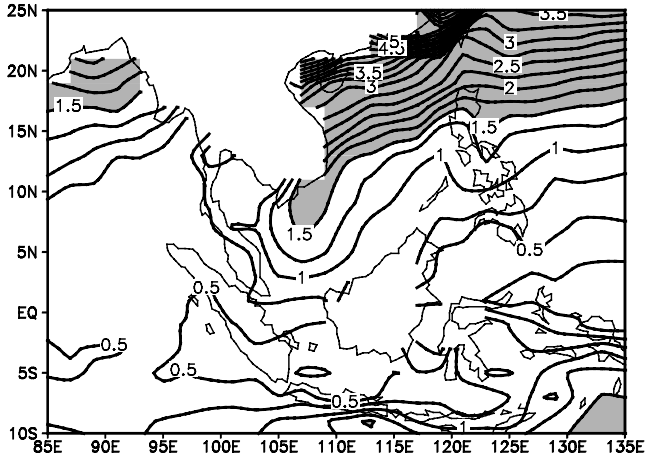

Figure 3. Annual harmonic of COADS SST climatology (°C).

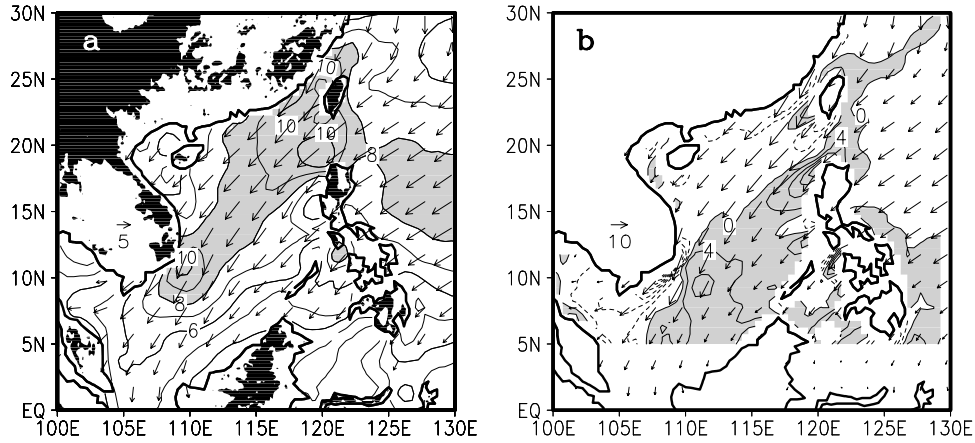

Figure 4. (a) QuikSCAT surface wind velocity (vectors) and its magnitude (contours at 2 m s^{-1} intervals; shading at >8 m s^{-1} intervals), averaged for December–February 2000–2002. (b) Surface wind stress (vectors in 0.1 N m^{-2}) and Ekman pumping velocity (contours at 4 $\times$ 10^{-6} m s^{-1} intervals; upwelling regions are shaded). The reference vector scales are 5 m s^{-1} and 10 $\times$ 10^{-2} N m^{-2} in Figures 4a and 4b, respectively. Land topography with elevations greater than 500 m is shaded in black in Figure 4a.

seasonal development of the cold tongue and its interannual variability, respectively. Section 5 is a summary.

2. Data

[6] Most of global climate data sets based on in situ observations and model assimilation are designed to study planetary-scale phenomena and are not suitable for studying smaller ocean basins such as the SCS. We use cloud-penetrating microwave satellite observations whose typical resolution (0.25°) is sufficiently high for our SCS study. Recent studies using these new satellite data sets have revealed new features of air-sea interaction near ocean fronts [*Liu et al.*, 2000; *Chelton et al.*, 2001; *Hashizume et al.*, 2001; *Nonaka and Xie*, 2003] and triggered by land orographic features [*Xie et al.*, 2001]. See *Xie* [2004] for a review of these recent satellite studies of air-sea interaction. In particular, a recent satellite study shows that the blockage of the southwest summer monsoon by the Indochina cordillera triggers a chain of air-sea interaction, resulting in an anticyclonic eddy east of South Vietnam that advects cold upwelled coastal water offshore to cause a basin-wide midsummer cooling of the SCS [*Xie et al.*, 2003].

[7] We use a suite of new satellite observations to gain a physically consistent picture of SCS climate in winter. The Tropical Rain Measuring Mission (TRMM) satellite's microwave imager (TMI) can see through clouds and substantially improve the sampling of SST over cloudy regions like the SCS [*Wentz et al.*, 2000; *Xie et al.*, 2003]. Here we use a monthly product available since December 1997 on a 0.25° grid. We supplement this TMI data set with SST climatology on a 9 km grid that is based on advanced very high resolution radiometer (AVHRR) infrared observations for a 15-year period of 1985–1999 [*Armstrong and Vazquez-Cuervo*, 2001]. AVHRR complements TMI observations in covering a longer period of time and coastal waters where TMI measurements are contaminated by land microwave emission.

[8] A sea surface height (SSH) data set that merge European Remote Sensing (ERS) and TOPEX/Poseidon (T/P) altimetry observations provides an improved space-time sampling [*Ducet et al.*, 2000]. This SSH product is available at a 10-day interval with a 0.25° $\times$ 0.25° resolution for the period from October 1992 to August 2001. Satellite altimeters observe only temporal deviations from the long-term mean SSH. To the merged T/P-ERS SSH anomalies, we add the annual-mean SSH climatology derived from the Parallel Ocean Climate Model (POCM) simulation for a 6-year period of 1993–1998 [*Semtner and Chervin*, 1992].

[9] The microwave scatterometer on the QuikSCAT satellite measures surface wind velocity over the world ocean on a daily basis [*Liu et al.*, 2000]. We construct a monthly climatology of wind stress from weekly QuikSCAT observations for August 1999 to June 2002 on a 0.5° grid. While having lower resolutions in space and time than QuikSCAT, ERS scatterometers operate for a longer period of time. To study interannual variability, we use a monthly mean ERS wind stress data set on a 1° grid from September 1991 to December 2000.

[10] Most of the above satellite observations are not available prior to early 1990s. To obtain robust statistics of interannual variability, we use the *Reynolds and Smith* [1994] monthly analysis of SST (NOAA OI.v2) from December 1981 to February 2003, available on a 1° grid (satellite infrared SST observations become operational in 1982). The Comprehensive Ocean and Atmosphere Dataset (COADS) surface net heat flux climatology on a 1° grid and the Japanese Ocean Flux datasets with Use of Remote sensing Observations (J-OFURO) surface net heat flux from October 1992 to September 1993 on a 1° grid are also used here. For monthly wind velocity at 850 hPa for the same period, we use the National Centers for Environmental Prediction/National Center for Atmospheric Research (NCEP/NCAR) Reanalysis [*Kalnay et al.*, 1996].

3. SCS Cold Tongue

3.1. Prevailing Winds, Ocean Circulation, and Their Effect on SST

[11] Figure 4 displays the climatological distributions of QuikSCAT wind vectors and Ekman pumping velocity for

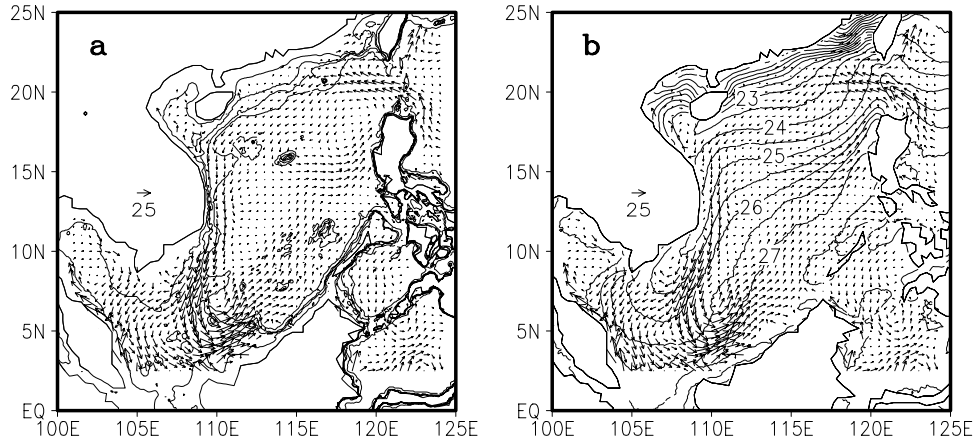

Figure 5. Geostrophic current climatology (vectors in 10^{-2} m s^{-1}) for November–January based on satellite altimetry observations, along with (a) bottom depth (contours at 50, 100, 200, and 1000 m) and (b) AVHRR SST climatology for December–February (contours in °C).

2000–2002, and the Ekman pumping velocity is calculated based the wind vectors [*Behera et al.* 1999]. In winter the northeasterly monsoon prevails in the SCS. There are localized wind maxima that exceed 10 m s^{-1}, each associated with orographic features on nearby land (Figure 4a). A wind speed maximum exceeding 10 m s^{-1} is found in the Taiwan Strait and the Luzon Strait as a result of orographic forcing by mountains on Taiwan and Luzon. The second wind maximum is located around 11°N off the coast of South Vietnam near the southern tip of Annam Cordillera, which is a mountain range that rises above 500 m and runs in a north-south direction on the east coast of Indochina Peninsula. The northeasterly winds are blocked by this coastal mountain range, giving rise to a wind jet offshore. This northeasterly winter jet is similar to the southwesterly summer jet [*Xie et al.*, 2003], except with the opposite wind direction.

[12] On the basin scale, wind speed reaches maximum (>8 m s^{-1}) along the southwest diagonal in the SCS; the distribution of wind results in dipole wind stress curl. This southwest diagonal divides the SCS into two parts, with Ekman upwelling and downwelling prevailing in the southeastern and northwestern basins, respectively (Figure 4b). Ekman upwelling occupies most of the deep SCS (depth > 200 m), driving a basin-scale cyclonic gyre. This distribution features of ocean current is also shown in seasonal average temperature and salinity data [*Qu*, 2000; *Liu et al.*, 2000].

[13] The winter-mean geostrophic currents based on the satellite and POCM SSH fields are calculated (Figure 5a). A southward coastal current develops to east of South Vietnam, increasing in intensity as it flows south. After leaving the Vietnam coast, this current continues southward, roughly following the 200 m bathymetry along the continental slope (the Sunda Slope) as the western boundary current (WBC) of the basin-scale cyclonic gyre. The maximum speed of this Sunda Slope Current approaches 0.5 m s^{-1} on seasonal mean (Figures 5a and 5b).

[14] While the winter gyre and its southward WBC have been studied previously on the basis of observations and numerical model simulations [*Xu et al.*, 1980; *Shaw and Chao*, 1994; *Shaw et al.*, 1999; *Chu et al.*, 1999; *Ho et al.*, 2000; *Qu*, 2000; *Yang et al.*, 2002], the southward WBC effect on the SST distribution has not been discussed in the literature. This SST effect is quite obvious in Figure 5b. A pronounced cold tongue develops near the continental slope on the eastern edge of the Sunda Shelf, apparently as a result of the southward advection of cold coastal water by the intense WBC. The slight westward shift of the cold tongue relative to the axis of the WBC is probably due to the advection of surface Ekman flow. The advection effect can be seen on the shelf as well, an SST front forms along 103°∼104°E, where the leaked branch of the main WBC is blocked by a bathymetric ridge (<60 m in Figure 1) on the Sunda Shelf.

[15] Besides the seasonal decrease in insolation, a huge amount of sensible and latent heat is lost to the atmosphere as the northeast monsoon advects cold and dry continental air mass over the SCS. The coldest SST is found on the northern boundary of the SCS both because the surface cooling is most intense and because of shallow bathymetry there. Under the same surface cooling, the shallower the depth, the more rapidly the water column cools. Within the SCS this bathymetric effect on SST is most clear in the Gulf of Beibu (Tonkin). where SST follows a tongue-like feature in the bathymetry. Over the shallow shelf seas to the north between China and Korea/Japan, bathymetric effect is even more evident in winter SST, imprinting on surface wind and cloud fields through air-sea interaction [*Xie et al.*, 2002].

3.2. Seasonal Development

[16] Climatological SST and geostrophic currents in September through November are shown in Figure 6. The September circulation bears the characteristics of the summer regime including a double-cell circulation straddling along 11°N. The strong eastward jet between the southern anticyclonic and northern cyclonic cells advects offshore cold water upwelled on the Vietnam coast, causing a basin-wide cooling in July and August [*Xie et al.*, 2003]. In September, relatively low SSTs (<28.5°C) can still be seen on the coast of South Vietnam and near the eastward current jet.

[17] During October the SCS circulation shifts from the summer to winter regime. The double-cell summer circulation begins to disintegrate, and a basin-wide cyclonic

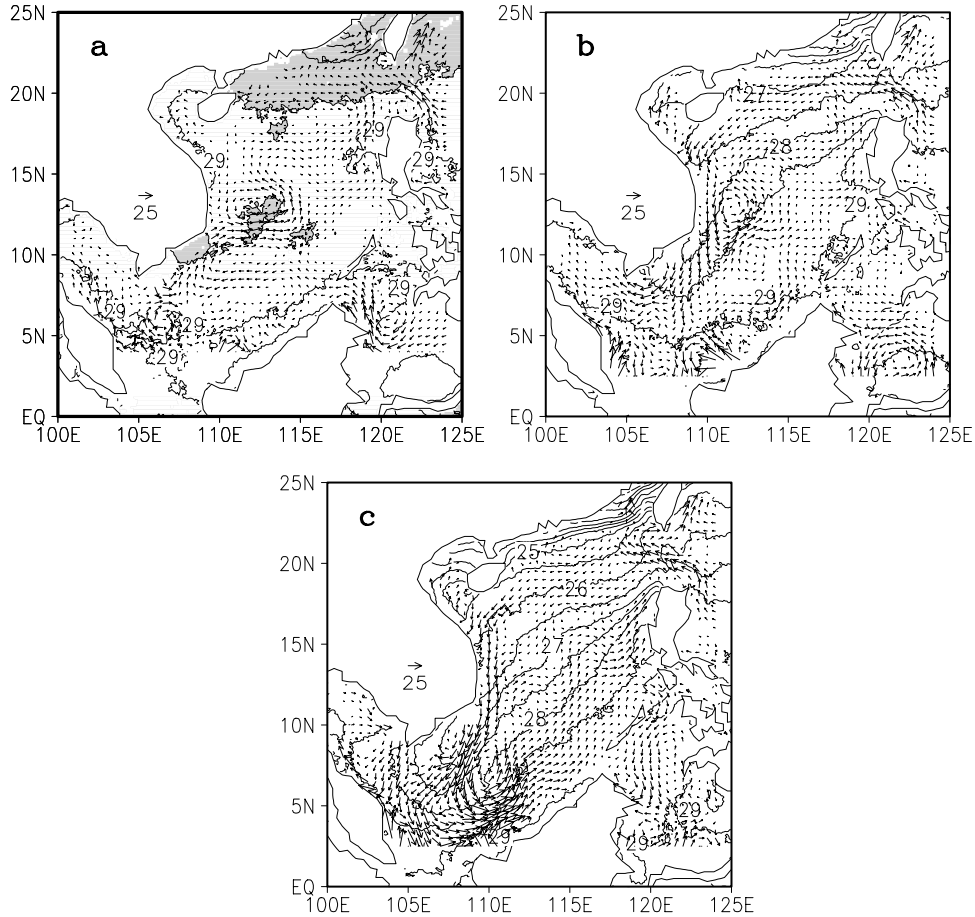

Figure 6. Geostrophic current (vectors in 10^{-2} m s^{-1}) and AVHRR SST climatology (contours in 0.5°C; shading < 28.5°C) for (a) September, (b) October, and (c) November.

circulation begins taking shape in response to the transition in atmospheric monsoon. A southward boundary current starts to appear on the coast of South Vietnam and on the continental slope between the deep SCS and Sunda Shelf. Associated with this development of the southward western boundary current, the cold tongue on the Sunda Slope advances south with the current. By November the southward current on the western boundary of the deep SCS is fully developed and so is the cold tongue on the continental slope in the southern basin.

[18] From October to November the SCS experiences a basin-wide cooling as a result of decreased solar radiation and increased turbulence heat flux from the ocean as the northeasterly monsoon sets in (Figure 7). The cooling rate

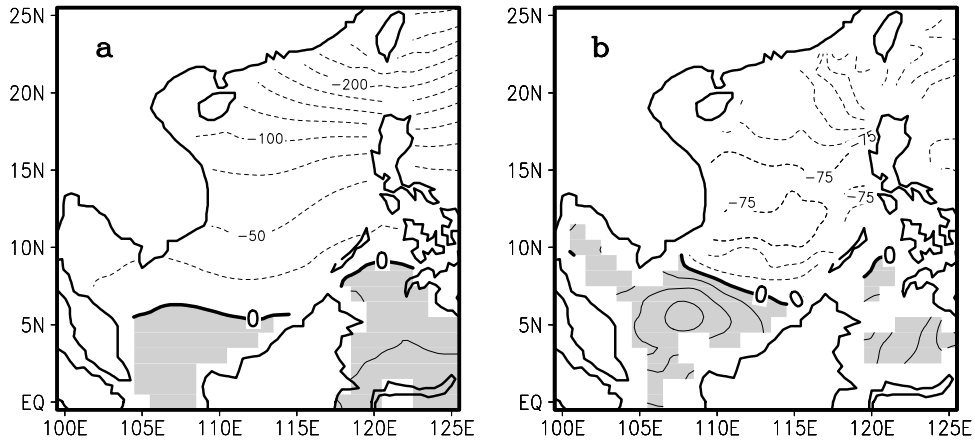

Figure 7. Net surface heat flux (W m^{-2}) averaged for November–January, based on (a) the COADS climatology and (b) J-OFURO for 1992–1993, the period for which the latter data set is available.

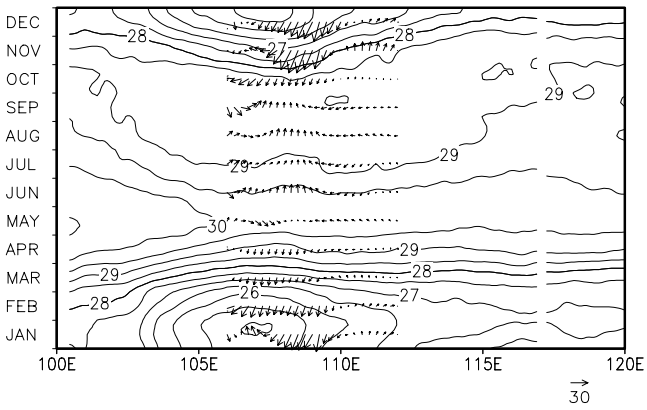

Figure 8. Longitude-time section of AVHRR SST climatology (contours in 0.5°C) and geostrophic current vectors (in 10^{-2} m s^{-1}, upward for northward flows) along 8°N.

due to the advection by the southward Sunda Slope current amounts to 1.3°C per month, for a typical current speed of 0.25 m s^{-1} and meridional SST gradient of 1°C per 500 km. With an annual average of mixed layer depth of 40 m [*Qu*, 2001] this advection cooling is equivalent to a surface heat flux of 80 W m^{-2}, which is much larger than the local net surface heat flux (∼25 W m^{-2}) in the southern SCS during winter (Figure 7a). Estimates of surface heat flux are subject to significant errors because of the uncertainties in estimating incoming solar radiation and turbulent heat flux. In a new heat flux data set that uses high-resolution satellite measurements (J-OFURO [*Kubota et al.*, 2002]) the November–January mean net flux is downward around the near the Sunda slope (Figure 7b), presumably resulting from both the suppression of surface turbulent heat flux by the development of the cold tongue and reduced cloud cover there (Figure 2b). This local maximum in downward heat flux is also visible in Figure 7a, which is based on the heavily smoothed COADS product. Thus the net effect of surface heat flux appears to be a damping against the cold advection by the slope current. Long-term, high-quality, and high-resolution heat flux data are necessary to test this hypothesis.

[19] Besides surface heat flux forcing and horizontal advection, vertical entrainment may also be important for mixed layer temperature tendency [e.g., *Qiu*, 2000]. Vertical entrainment is important for cooling associated with the southwest monsoon in summer, but it is negative during the northeast monsoon in some parts of the SCS (Figure 8) [*Qu*, 2001]. In fact, according the current speed of 0.25 m s^{-1} and meridional SST gradient of 1°C per 500 km the southward cold advection (−1.3°C per month) accounts for 85% of the total decreases in SST (∼1.5°C) in the cold tongue from November to December. This estimate of the relative importance of the southward cold advection is consistent with the visual inspection that SST reaches a distinct minimum in the cold tongue.

[20] The longitude-time section (along 8°N) of SST and current captures the seasonal development of the cold tongue (Figure 8). Here the cold tongue appears as a zonal SST minimum centered at 107°E, with values 2°C lower than the ambient. A weak SST minimum forms at this longitude as soon as the first sign of the southward boundary current appears in October. This western boundary current is the strongest in November–January, resulting in an intensification of the cold tongue. The systematic westward shift of the center of the cold tongue relative to the southward current maximum is probably due to the advection by the northwestward surface Ekman flow. SST in both the deep SCS and cold tongue reaches a seasonal minimum in late January to early February. The southward boundary current begins to weaken in February and so does the cold tongue. With the increase in solar radiation and decrease in wind speed the SCS starts to warm up from February, and its SST reaches a seasonal maximum in May before the onset of the southwesterly monsoon.

4. Interannual Variability

[21] The SCS displays considerable interannual variability [e.g., *Wang et al.*, 2002]. This section investigates its time-space structure and relationships with the SCS cold tongue and other global-scale variability by statistical analysis.

4.1. Role of the SCS Cold Tongue

[22] Figure 9a depicts the root-mean-square (RMS) variance of interannual SST variability in December–February based on the 1° × 1° *Reynolds and Smith* [1994] analysis for a 22-year period of 1982–2003. There is a local maximum in the RMS SST variance in the southern SCS in 5°∼10°N, 106°∼111°E that is almost collocated with the climatological cold tongue on the Sunda Slope. The RMS

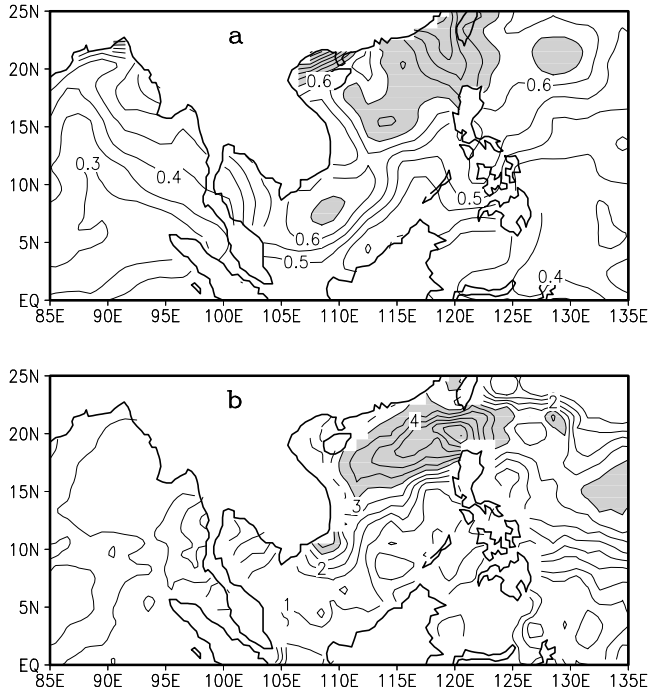

Figure 9. Root-mean-square variance (a) SST (°C) and (b) wind stress (10^{-2} N m^{-2}) in winter, based on the Reynolds-Smith SST data set from December 1981 to February 2003 and ERS satellite wind observations for September 1991 to December 2000.

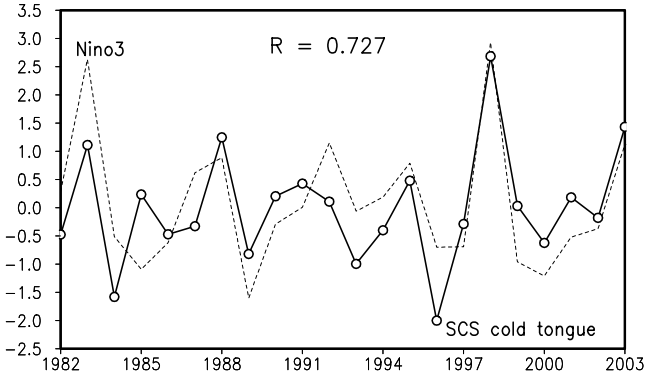

Figure 10. The winter cold tongue index (solid line with open circles) and the December Nino3 SST (dashed line), normalized by their respective RMS variance (0.58 and 1.27°C). The correlation of the two time series is 0.727.

variance in this region is ∼60% greater than that in either the eastern Indian Ocean to the west or the western Pacific to the east at the same latitude. In this latitude band the ERS wind speed shows similar levels of variability in the eastern Indian Ocean, SCS, and western Pacific (Figure 9b). (The maximum wind speed variance is located over or slight north of the axis of the mean winter monsoon.) Thus variability in the southward western boundary current on the Sunda Slope may play an important role in producing the locally enhanced SST variance.

[23] Why does a local maximum in the RMS SST and wind speed variance appear in the center of the SCS cold tongue during winter? To further study interannual variability, we define a SCS cold tongue (SCT) index by averaging SST anomaly in the high-variance region (5°∼10°N, 106°∼111°E) and for December–February, which is normalized by its RMS variance (0.58°C). The SCT index is strongly correlated with December SST anomalies in the eastern equatorial Pacific (Figure 10). The intervals between neighboring SCS warm events are 2–4 years, similar to those of the ENSO index. Their correlation coefficient amounts to 0.73 during 1982–2003 (0.423 is 95% significant for 20 degrees of freedom).

[24] The distributions of correlations with the SCT index of surface wind stress, Ekman pumping velocity, SSH, geostrophic current, and SST are shown in Figure 11. An anomalous warming in the SCS cold tongue is associated

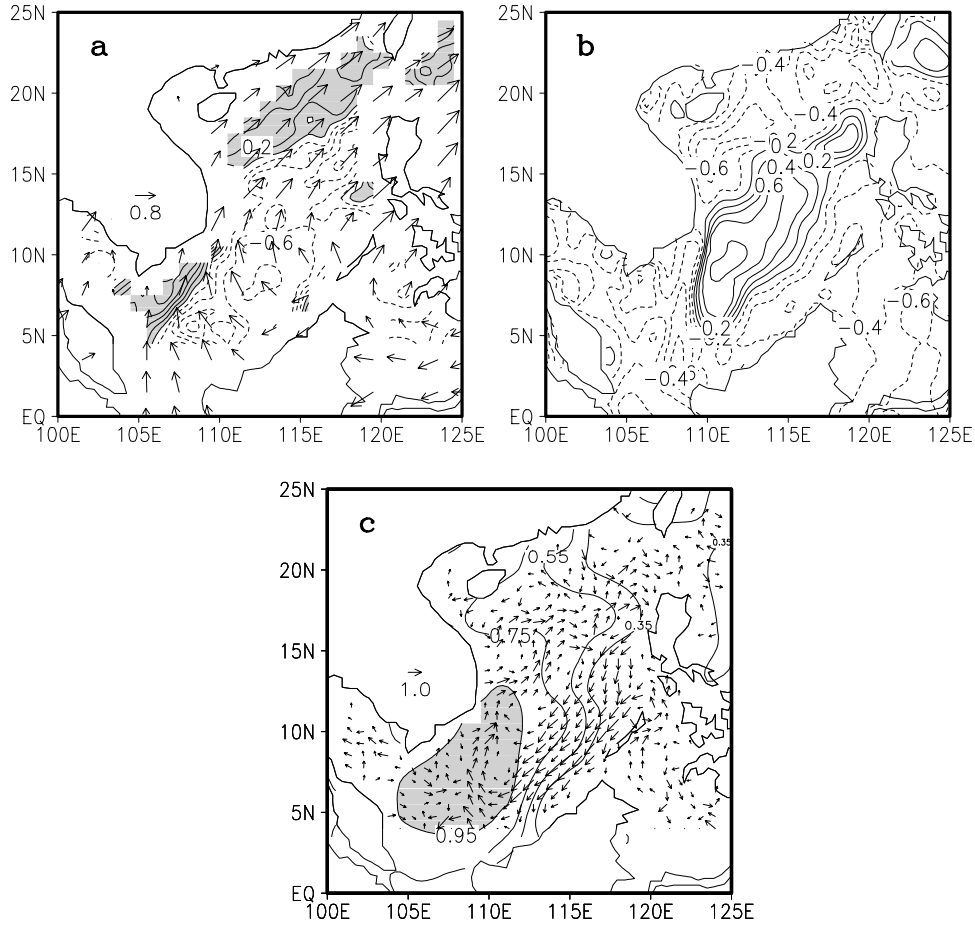

Figure 11. Correlations with the winter SCS cold tongue index: (a) ERS wind stress (vectors) and Ekman pumping velocity (contours) (0.707 is 95% significant for 6 degrees of freedom), (b) SSH (contours), and (c) geostrophic current (vectors) and SST (contours) (0.666 is 95% significant for 7 degrees of freedom in Figures 11b and 11c). In Figures 11a and 11c the zonal (meridional) component of a vector shows the correlation coefficient of the zonal (meridional) component of the velocity vector with SCS cold tongue index at that grid point.

with a weakened winter monsoon. Anomalous Ekman downwelling dominates the southern SCS except over the Sunda Shelf. This reduced Ekman pumping weakens the cyclonic basin-wide circulation through the Rossby wave adjustment because the intensity of the gyre in the basin-wide depends on the Ekman pumping [*Z. Liu et al.*, 2001]. The anomalous ocean circulation is characterized by a rise in SSH in the central SCS and reduced SSH along the boundaries. Overall, SSH anomalies are quite consistent with those of Ekman pumping velocity anomaly, negative SSH anomalies over positive Ekman pumping anomalies and vice versa. This SSH correlation pattern indicates a weakened southward boundary current on the Sunda Slope, and this reduced cold advection causes the cold tongue to warm up. This covariability of the western boundary current and cold tongue further supports the notion discussed in section 3 that the former causes the latter.

[25] In the anomalously warm winter of 1997/1998 the southward western boundary current on the Sunda Slope decreases to $\sim$0.15 m s^{-1} (from a climatological mean of 0.25 m s^{-1}). With a meridional SST gradient of 1°C per 500 km the reduced western boundary current will increase the SST in the SCT by 1.5°C in 3 months (from November to January), a number comparable to the observed SCT anomaly ($\sim$1.5°C) in 1997/1998 winter (Figure 10). In the anomalously cold winter of 1995/1996 the southward western boundary current is $\sim$0.32 m s^{-1}, and the SCT index anomaly is -1°C (Figure 10).

[26] Large anomalies of geostrophic currents are found on the southeastern boundary of the SCS. The cold advection by these southwestward current anomalies counteracts the warming due to the weakened monsoon and reduced surface turbulence heat flux from the ocean. The opposing effects of geostrophic advection and surface heat flux forcing seem to be the reason for small SST variability in the southeastern SCS west of the southern Philippines and Borneo (Figure 9a).

4.2. Correlation With ENSO

[27] Wind anomalies over the SCS as depicted in Figure 11a are part of the planetary-scale atmospheric circulation changes associated with ENSO. Figure 12 shows the correlations of SST, 850 hPa winds, and rainfall with the Nino3 SST index in December. At the height of an El Niño (which peaks in December), positive SST anomalies occupy the equatorial Pacific east of the date line, while negative ones are found over much of the rest of the tropical Pacific and over the tropical Indian Ocean. Rainfall anomalies are characterized by a zonal dipole with rainfall increasing over the central and eastern Pacific and decreasing over the Indo-Pacific warm pool. There is a pair of anticylonic circulations astride the equator over the Indo-western Pacific oceans, presumably as the Rossby response to rainfall anomalies. The weakened northeast monsoon over the SCS is part of the northern anticyclonic circulation that extends from the Indian Ocean to the date line.

[28] To first order, the anticyclonic anomalous circulations over the Indo-western Pacific, and the weakened northeast monsoon over the SCS, are the atmospheric response to Pacific SST anomalies of El Niño by the so-called "atmospheric bridge" mechanism (see *Alexander et al.* [2002] for a recent review). An atmospheric general circulation model

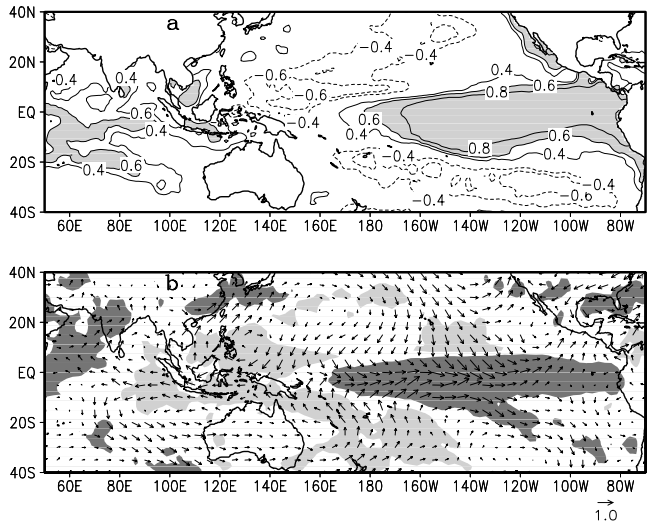

Figure 12. Simultaneous correlations with the Nino3 SST index in December of (a) SST (contours; shading >0.6) and (b) wind velocity at 850 hPa (vectors) and precipitation (dark shading >0.413; light shading <−0.413), based on the Reynolds-Smith SST for 1982–2003 (0.423 is 95% significant for 20 degrees of freedom), the NCEP/NCAR reanalysis for 1959–1997 (0.317 is 95% significant for 37 degrees of freedom), and the CPC Merged Analysis of Precipitation data from January 1979 to June 2002 (0.413 is 95% significant for 21degree of freedom), respectively.

captures the subtropical anticyclonic circulations over the Indo-western Pacific in simulations forced with SST anomalies in the tropical Pacific east of the date line [*Lau and Nath*, 2000]. When an ocean mixed layer model is implemented elsewhere and coupled with the atmospheric model [*Alexander et al.*, 2002], the Indian Ocean warming is well simulated except along 10°S where the thermocline is shallow and ocean waves are a major mechanism for SST variability [e.g., *Xie et al.*, 2002].

[29] As discussed in section 4.1, the weakened winter monsoon causes the cyclonic SCS circulation to spin down, which decelerates the western boundary current and reduces its cold advection. This change in the western boundary current results in a warming in the cold tongue on the Sunda Slope. Indeed, the SST correlation with ENSO features a local maximum near the climatological SCS cold tongue, higher than in either the Indian or western Pacific north of the equator. The atmospheric anticyclonic circulation forms in winter and persists into summer [*Wang et al.*, 2000], giving rise to a summer warming over the SCS [*Xie et al.*, 2003]. As a result, climatic anomalies in both the atmosphere and SST over the SCS tend to persist for about a year during and following an El Niño.

[30] Finally, we comment briefly on SST variability west of the Luzon Strait, which is noticeably greater in amplitude than in the southern cold tongue. Curiously, SST anomalies there are not correlated with either the SCS cold tongue variability or ENSO, but wind velocity in the same region is (Figures 11 and 12). Preliminary analysis of SSH observations indicates that SST anomalies to west of the Luzon Strait are associated with variability in Kuroshio intrusion

(not shown), another example of ocean current effects on SCS climate variability.

5. Summary and Discussion

[31] Recent satellite remote sensing technology is revolutionizing ocean observations, enabling us to make routine measurements of SST and surface winds at high resolution over the world ocean. Taking advantage of these new satellite observations, we have investigated the spatial distribution of SST and its interannual variations in the SCS and the overlying atmosphere in boreal winter. The northeast monsoon prevails in the winter SCS, causing Ekman pumping in the southeastern half of the basin. This Ekman pumping spins up a cyclonic circulation over the SCS, with a southward western boundary current on the coast of South Vietnam and the continental slope east of the Sunda Shelf. This southward flow amounts to a speed as much as 0.5 m s^{-1} in the 10-year climatology, advecting cold water from the north to form a distinct cold tongue in the SST climatology along the Sunda Slope. This cold tongue is not collocated with the southward ocean jet but is displaced to the northwest probably because of the advection by the surface Ekman flow. This cold tongue is fully developed in November–February and then dissipates as the northeast monsoon recedes.

[32] Interannual SST variance reaches a local maximum along this climatological cold tongue on the Sunda Slope. The interannual variability of this winter cold tongue is highly correlated with ENSO. As an El Niño in the Pacific reaches its peak in winter, the northeast monsoon weakens over the SCS as part of the anomalous anticylonic circulation that dominates the lower troposphere over the SCS-western North Pacific in response to enhanced convection in the central equatorial Pacific. The weakened winter monsoon is associated with a spin down of the SCS circulation and a deceleration of its western boundary current. The reduced thermal advection by this current leads to a warming in the cold tongue on the Sunda Slope.

[33] Together with *Xie et al.* [2003], our results suggest that ocean dynamics in general and thermal advection by ocean currents in particular play an important role in the formation of SST climatology and its interannual variability over the SCS. These two studies further show that ENSO is a major forcing for regional climate variability as reflected in monsoon and SST variations. During and after an El Niño the SCS is anomalously warm, and SST anomalies are particularly large over the Sunda Slope cold tongue in winter and east of South Vietnam in summer. The long persistence of SCS SST anomalies is rooted in the persistence of the atmospheric anticyclone over the SCS-western Pacific region, with the latter's cause remaining to be studied.

[34] **Acknowledgments.** We would like to thank Qiang Xie for providing the AVHRR data set, Jan Hafner for maintaining a satellite database that this study draws on, and Robin Tokmakian and Peter Braccio for the POCM output. The merged SSH data set is obtained from the Collecte Localisation Satellites, AVISO, France; TMI data are from Remote Sensing Systems; QuikSCAT and AVHRR data are from JPL; and ERS data are from the Institute FranÇais de Recherche pour l'Exploitation de la Mer. This work is supported by Special Program 2001DIA50041 from Ministry of Science and Technology of China, Natural Science Foundation of China (40240420564 and 40233033), NASA, and Frontier Research System for Global Change. IPRC contribution 280 and SOEST contribution 6403.

References

Alexander, M. A., I. Blade, M. Newman, J. R. Lanzante, N.-C. Lau, and J. D. Scott (2002), The atmospheric bridge: The influence of ENSO teleconnections on air-sea interaction over the global oceans, *J. Clim.*, *15*, 2205–2231.

Armstrong, E. M., and J. Vazquez-Cuervo (2001), A new global satellite-based sea surface temperature climatology, *Geophys. Res. Lett.*, *28*, 4199–4202.

Behera, S. K., D. W. Ganer, and R. S. K. Singh (1999), An investigation of Ekman pumping velocity and mixed layer depth in the Indian Ocean, in *Advanced Technologies in Meteorology (TROPMET '99)*, edited by R. K. Gupta and S. J. Reddy, McGraw-Hill, New York. (Available at http://www.commonwealthknowledge.net/MetCD/Chapter4/C4P09.htm)

Chelton, D. B., S. K. Esbensen, M. G. Schlax, N. Thum, M. H. Freilich, F. J. Wentz, C. L. Gentemann, M. J. McPhaden, and P. S. Schopf (2001), Observations of coupling between surface wind stress and sea surface temperature in the eastern tropical Pacific, *J. Clim.*, *14*, 1479–1498.

Chu, P. C., N. L. Edmons, and C. Fan (1999), Dynamical mechanisms for the South China Sea seasonal circulation and thermohaline variabilities, *J. Phys. Oceanogr.*, *29*, 2971–2989.

Ducet, N., P. Y. Le Traon, and G. Reverdin (2000), Global high-resolution mapping of ocean circulation from TOPEX/Poseidon and ERS-1 and -2, *J. Geophys. Res.*, *105*, 19,477–19,498.

Hashizume, H., S. P. Xie, W. T. Liu, and K. Takeuchi (2001), Local and remote atmospheric response to tropical instability waves: A global view from the space, *J. Geophys. Res.*, *106*, 10,173–10,185.

Ho, C. R., Q. Zheng, Y. S. Soong, N. J. Kuo, and J. H. Hu (2000), Seasonal variability of sea surface height in the South China Sea observed with TOPEX/Poseidon altimeter data, *J. Geophys. Res.*, *105*, 13,981–13,990.

Kalnay, E., et al. (1996), The NCEP/NCAR 40-year re-analysis project, *Bull. Am. Meteorol. Soc.*, *77*, 437–471.

Kubota, M., N. Iwasaka, S. Izu, M. Konda, and K. Kutsuwada (2002), Japanese ocean flux data sets with the use of remote sensing observations (J-OFURO), *J. Oceanogr.*, *58*, 213–225.

Lau, N.-C., and M. J. Nath (2000), Impact of ENSO on the variability of the Asian-Australian monsoons as simulated in GCM experiments, *J. Clim.*, *13*, 4287–4308.

Li, L., R. Wu, and X. Guo (2000), Seasonal circulation in the South China Sea: An application study of satellite altimeter TOPEX/Poseidon (in Chinese), *Acta Oceanol. Sin.*, *22*, 13–26.

Liu, Q., W. Li, and Q. Xu (1997), Interaction between northeaster and ocean circulation in winter (in Chinese), *Oceanol. Limnol. Sin.*, *28*, 493–502.

Liu, Q., H. Yang, and Q. Wang (2000), Dynamic characteristics of seasonal thermocline in the deep sea region of the South China Sea, *Chin. J. Oceanol. Limnol.*, *18*(2), 104–109.

Liu, Q., H. Yang, and Z. Liu (2001), Seasonal features of the Sverdrup circulation in the South China Sea, *Progr. Nat. Sci.*, *11*, 202–206.

Liu, W. T., and X. Xie (1999), Space-based observations of the seasonal changes of South Asian monsoons and oceanic response, *Geophys. Res. Lett.*, *26*, 1473–1476.

Liu, W. T., X. Xie, P. S. Polito, S.-P. Xie, and H. Hashizume (2000), Atmospheric manifestation of tropical instability waves observed by QuikSCAT and Tropical Rain Measuring Mission, *Geophys. Res. Lett.*, *27*, 2545–2548.

Liu, Z., H. Yang, and Q. Liu (2001), Regional dynamics of seasonal variability in the South China Sea, *J. Phys. Oceanogr.*, *31*, 272–284.

Nonaka, M., and S.-P. Xie (2003), Co-variations of sea surface temperature and wind over the Kuroshio and its extension: Evidence for ocean-to-atmospheric feedback, *J. Clim.*, *16*, 1404–1413.

Qiu, B. (2000), Interannual variability of the Kuroshio extension system and its impact on the wintertime SST field, *J. Phys. Oceanogr.*, *30*, 1486–1502.

Qu, T. (2000), Upper-layer circulation in the South China Sea, *J. Phys. Oceanogr.*, *30*, 1450–1460.

Qu, T. (2001), Role of ocean dynamics in determining the mean seasonal cycle of the South China Sea surface temperature, *J. Geophys. Res.*, *106*, 6943–6955.

Reynolds, R. W., and T. M. Smith (1994), Improved global sea surface temperature analyses using optimal interpolation, *J. Clim.*, *7*, 929–948.

Semtner, A. J., and R. M. Chervin (1992), Ocean general circulation from a global eddy-resolving model, *J. Geophys. Res.*, *97*, 5493–5550.

Shaw, P. T., and S. Y. Chao (1994), Surface circulation in the South China Sea, *Deep Sea Res., Part I*, *41*, 1663–1683.

Shaw, P. T., S. Y. Chao, and L. Fu (1999), Sea surface height variations in the South China Sea from satellite altimetry, *Oceanol. Acta*, *22*, 1–17.

Wang, B., R. Wu, and X. Fu (2000), Pacific-East Asian teleconnection: How does ENSO affect east Asian climate?, *J. Clim.*, *13*, 1517–1536.

Wang, D., Q. Xie, Y. Du, W.-Q. Wang, and J. Chen (2002), The 1997–1998 warm event in the South China Sea, *Chin. Sci. Bull.*, *47*, 1221–1227.

Wentz, F. J., C. Gentemann, D. Smith, and D. Chelton (2000), Satellite measurements of sea surface temperature through clouds, *Science*, *288*, 847–850.

Wyrki, K. (1961), Physical oceanography of the Southeast Asian waters: Scientific results of marine investigations of the South China Sea and the Gulf of Thailand, *NAGA Rep. 2*, 195 pp., Scripps Inst. of Oceanogr., La Jolla, Calif.

Xie, S.-P. (2004), Satellite observations of cool ocean-atmosphere interaction, *Bull. Am. Meteorol. Soc.*, *85*, 195–208.

Xie, S.-P., W. T. Liu, Q. Liu, and M. Nonaka (2001), Far-reaching effects of the Hawaiian Islands on the Pacific Ocean-atmosphere, *Science*, *292*, 2057–2060.

Xie, S.-P., J. Hafner, Y. Tanimoto, W. T. Liu, H. Tokinaga, and H. Xu (2002), Bathymetric effect on the winter sea surface temperature and climate of the Yellow and East China Seas, *Geophys. Res. Lett.*, *29*(24), 2228, doi:10.1029/2002GL015884.

Xie, S.-P., Q. Xie, D. X. Wang, and W. T. Liu (2003), Summer upwelling in the South China Sea and its role in regional climate variations, *J. Geophys. Res.*, *108*(C8), 3261, doi:10.1029/2003JC001867.

Xu, X., Z. Qiu, and H. Cheng (1980), A survey of the circulation of the SCS (in Chinese), in *Proceedings of the Chinese Oceanography and Limonology Conference on Hydrological Meteorology*, pp. 137–145, Science, Beijing.

Yang, H., Q. Liu, Z. Liu, D. Wang, and X. Liu (2002), A general circulation model study of the dynamics of the upper ocean circulation of the South China Sea, *J. Geophys. Res.*, *107*(C7), 3085, doi:10.1029/2001JC001084.

Q. Liu and X. Jiang, Physical Oceanography Laboratory, Ocean University of China, Number 5, Yushan Road, Qingdao 2666003, China. (liuqy@ouc.edu.cn)

W. T. Liu, Jet Propulsion Laboratory, MS 300-323, Pasadena, CA 91109-8099, USA. (liu@pacific.jpl.nasa.gov)

S.-P. Xie, International Pacific Research Center, SOEST, University of Hawaii, Honolulu, HI 96822, USA. (xie@hawaii.edu)